EXPERIMENTAL VERIFICATION OF MULTI-PHYSICAL MODELLING OF THE KEYHOLE LASER WELDING PROCESS

801

B.J. Aalderink[1], D.F. de Lange[1], R.G.K.M. Aarts[2] and J. Meijer[2]

[1] Netherlands Institute for Metals Research
P.O. Box 217, 7500 AE Enschede, The Netherlands
[2] University of Twente, Laboratory of Mechanical Automation
P.O. Box 217, 7500 AE Enschede, The Netherlands

b.aalderink@nimr.nl

Abstract

To investigate the influence of temperature dependant material properties on model results, 2D FEM calculations for thin sheets of AA5182 aluminium alloy were compared with real-time coaxial camera images of the laser welding process. The results show the importance of taking into account the latent heat of the solid-liquid phase transition in the model. Including temperature dependant values of the thermal conductivity and the specific heat slightly improved the model accuracy. The tendency of a shortening melt pool for higher values of the laser power could not be explained by this 2D model and is expected to be caused by a changing keyhole shape. In the FEM model results, the melt flow shows a clear recirculation with melt flowing forward on the centerline, from the tail region towards the keyhole.

Introduction

To obtain first-time-right high quality joints, it is essential to have models that can predict the welding behavior. Due to the highly non-linear nature of the laser keyhole welding process, it is difficult to model the behavior accurately.

Many models for the keyhole laser welding process have been proposed (e.g. [1, 2, 3, 4]). Some of these model results match quite well with experimental results, but are very complex and computationally intensive. Other models are less complex, but give no accurate predictions of the weld pool geometry.

In this paper a time-invariant 2D Finite Elements Method (FEM) model is discussed, which runs on a PC [5]. This model solves the temperature profile in and around the weld zone. Also the fluid flow in the melt pool is taken into account.

The model is verified for the laser welding process of 1.1 mm thick AA5182-O/H111 sheets. Using a special monitoring system, clear real-time images of the melt pool were captured. Contours of the melt pool predicted by the model were compared to camera images of the welding process.

Finite Element Model

The computational domain of the 2D model is given in Figure 1. The domain has been divided into three sub-domains. In domain Ω_1 only solid material is present. Domain Ω_2 represents an area in which both solidified and molten material are present. The boundary of the solid-liquid interface is not tracked using a free surface, but is indicated by the melt isotherm. Domain Ω_3 represents the laser spot. This is the area where the laser energy enters the computational domain.

Thermal Model

During welding the temperature has a strong influence on the resulting weld quality. The heat balance equation can be written as

$$\rho c_p \frac{\partial T}{\partial t} = q(\mathbf{x}, t) z_1(T) + \nabla \cdot \lambda \nabla T - \rho c_p \mathbf{u} \cdot \nabla T \quad (1)$$

where ρ is the density [kg/m^3], c_p is the specific heat (including the latent heat, see Equation 3) [J/(kg K)] and λ is the thermal conductivity [W/(m K)]. In general all material parameters are a function of temperature T. The temperature dependency of c_p and λ is taken into account in the model. A change in density due to a temperature variation is compensated by an accompanied change in volume due to thermal expansion, together guaranteeing conservation of mass. Since volumetric expansion is not

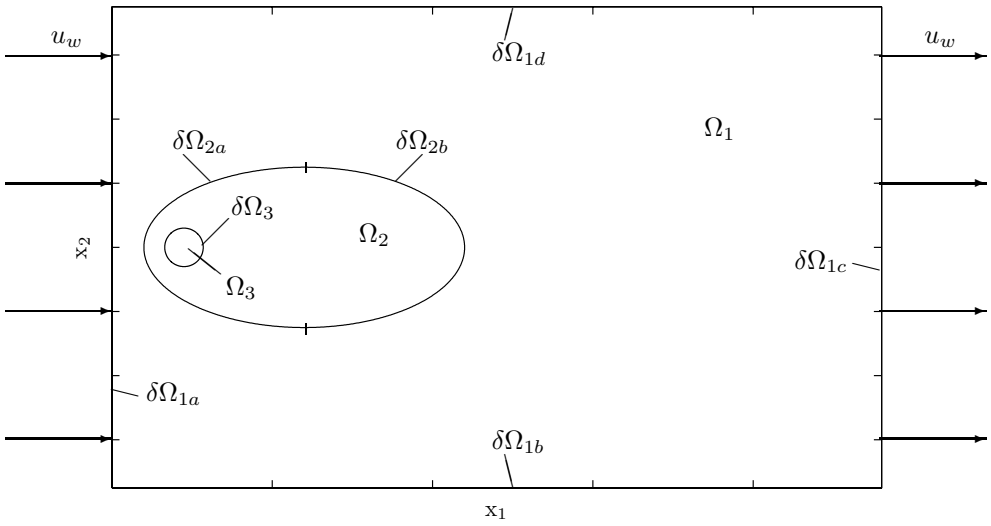

Figure 1: *The computational domain of the FEM model.*

taken into account in this model, the density is kept constant.

Furthermore, $q(\mathbf{x}, t)$ is a heat source as a function of space $\mathbf{x}$ and time t. The heat source is multiplied by a clipping function $z_1(T)$, which cuts off the energy flux above a certain temperature level, reflecting the loss of energy through the bottom keyhole opening. The temperature dependent function $z_1(T)$ has the value 1 when $T \leq T_b$ and 0 for $T > T_b$, where T_b is the boiling temperature. The heat loss due to evaporation is negligible and therefore omitted [3, 6].

It is computationally favorable to rewrite Equation 1 using dimensionless parameters using characteristic values for the temperature (T_0), the length scale (L_0), the velocity (U_0), the density (ρ_0), the heat capacity (c_{p_0}), the thermal conductivity coefficient (λ_0) and the heat source (q_0), giving

$$\begin{aligned}\tilde{\rho}\tilde{c_p}\frac{\partial \tilde{T}}{\partial \tilde{t}} = &\frac{L_0 q_0}{\rho_0 c_{p_0} U_0 T_0}\tilde{q}(\tilde{\mathbf{x}}, \tilde{t})\tilde{z_1}(\tilde{T}) + \\ &\tilde{\nabla}\cdot\frac{\lambda_0}{\rho_0 c_{p_0} U_0 L_0}\tilde{\lambda}\tilde{\nabla}\tilde{T} - \tilde{\rho}\tilde{c_p}\tilde{\mathbf{u}}\cdot\tilde{\nabla}\tilde{T}.\end{aligned} \tag{2}$$

Here $\tilde{a}$ refers to a dimensionless version of parameter a.

In this paper, a steady-state solution is calculated, which means that the left-hand side of Equation 2 is set to zero.

The effect of latent heat due to the solid liquid phase transformation is incorporated by increasing the specific heat between the solidus and liquidus temperatures [5] (Figure 5)

$$\begin{aligned} c_p(T) &= C_p(T) + h(T) \\ dH &= \int h(T) dT, \end{aligned} \tag{3}$$

where $h(T)$ is the latent heat as a function of temperature and $C_p(T)$ is the specific heat as a function of temperature, without the latent heat.

To solve the heat balance equation, boundary conditions need to be defined. The material that enters the computational domain through boundary $\delta\Omega_{1a}$ is set to room temperature T_r. On boundaries $\delta\Omega_{1b..d}$ the heat loss due to conduction is expected to be negligible.

$$\begin{aligned} T &= T_r \quad &\text{at} \quad \delta\Omega_{1a} \\ \mathbf{n}\cdot\nabla T &= 0 \quad &\text{at} \quad \delta\Omega_{1b..d} \end{aligned} \tag{4}$$

where $\mathbf{n}$ is the normal vector of the specific boundary.

Hydrodynamical Model

To incorporate the effects of the melt flow in the model, the velocity field in the melt pool needs to be determined. This can be done using the incompressible Navier-Stokes equations

$$\begin{aligned} \rho\frac{\partial \mathbf{u}}{\partial t} &= -\rho\mathbf{u}\cdot\nabla\mathbf{u} - \nabla p + \nabla\cdot\mu\left(\nabla\mathbf{u} + (\nabla\mathbf{u})^T\right) + \mathbf{F} \\ \nabla\cdot\mathbf{u} &= 0. \end{aligned} \tag{5}$$

Here p is the pressure [Pa], μ is the dynamic viscosity [kg/(m s)] and $\mathbf{F}$ are the external volume forces [N]. The dimensionless form of Equations 5 can be derived by defining additional characteristic quantities for viscosity (μ_0), pressure (p_0) and force (F_0), yielding

$$\begin{aligned}\tilde{\rho}\frac{\partial\tilde{\mathbf{u}}}{\partial\tilde{t}} &= -\tilde{\rho}\tilde{\mathbf{u}}\cdot\tilde{\nabla}\tilde{\mathbf{u}} - \frac{p_0}{\rho_0 U_0^2}\tilde{\nabla}\tilde{p} + \\ &\quad \tilde{\nabla}\cdot\frac{\mu_0}{\rho_0 L_0 U_0}\tilde{\mu}\left(\tilde{\nabla}\tilde{\mathbf{u}} + (\tilde{\nabla}\tilde{\mathbf{u}})^T\right) + \frac{L_0 F_0}{\rho_0 U_0^2}\tilde{\mathbf{F}} \\ \tilde{\nabla}\cdot\tilde{\mathbf{u}} &= 0.\end{aligned} \tag{6}$$

Various modelling approaches were tested to describe the presence of the keyhole. Although the various models show differences in the calculated temperature and flow fields, good results are obtained with a rather simple, straightforward model. This keyhole model uses an external force $\mathbf{F}$ to describe both the solidification of the melt and the presence of the keyhole. This force $\mathbf{F}$ is defined as

$$\mathbf{F} = (u_w\mathbf{e}_x - \mathbf{u})c_s z_2(T) - \mathbf{u}c_k z_3(T) \tag{7}$$

Here, the temperature dependant functions $z_2(T)$ and $z_3(T)$ are switching functions which activate or deactivate the respective terms. The first term simulates the solidification effect, since the external volume force forces the solidified material to move with the welding speed. Function $z_2(T)$ makes that this force is present when the temperature is below the solidus temperature T_s and disappears when T is over the liquidus temperature T_l, showing a smooth behavior in the region of $T_s < T < T_l$. The second term introduces a force which pushes the velocity to zero, causing a zone of stagnant melt which behaves as an object in the melt, representing the keyhole. The function $z_3(T)$ equals 1 for $T > T_b$ and 0 for $T < T_b$, with a smoothed transition around the boiling temperature T_b for numerical reasons. The constants c_k and c_s are tuning parameters to control the amplitude of the different force terms.

Since the Navier-Stokes equations are only solved in domain Ω_2 and Ω_3, the boundary conditions are formulated as follows

$$\begin{aligned}\mathbf{u} &= u_w\mathbf{e}_x \quad \text{at} \quad \delta\Omega_{2a} \\ p &= 0 \quad \text{at} \quad \delta\Omega_{2b}\end{aligned} \tag{8}$$

Experimental Setup

Welding experiments were carried out to compare the estimated melt contour with recorded camera images using a monitoring system [7]. In Figure 2 a schematic overview of this system is displayed. The high power Nd:YAG laser beam is focussed onto the sample surface by means of a collimation lens and a focussing lens. An off-axis mounted, fiber coupled diode laser illuminates the weld pool during the welding process. The light from the welding area is directed towards a camera by means of a dichroic mirror inside the welding head. A narrow bandpass optical filter that matches the wavelength of the diode laser light is placed in front of the camera

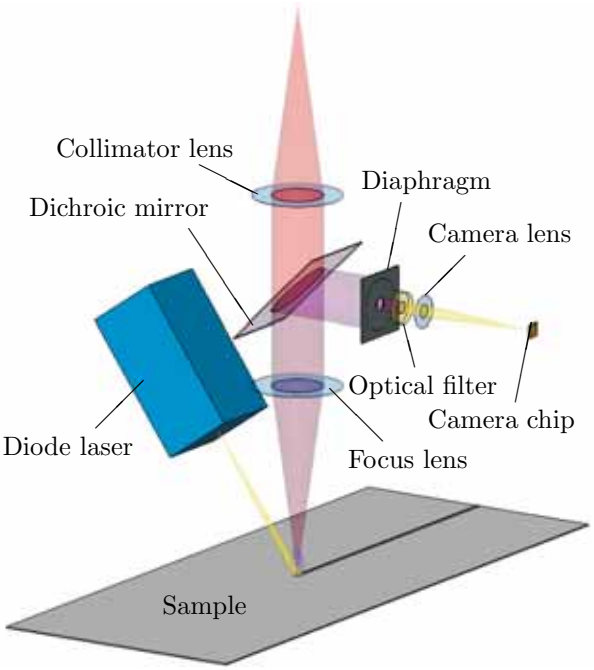

Figure 2: *A schematic overview of the coaxial monitoring system with external illumination.*

Seam configuration	Bead-on-plate
Plate thickness	1.1 mm
Laser light wavelength	1064 nm
Laser power (CW)	2500-4000 W
Welding speed	100-200 mm/s
Shielding gas	Ar
Shielding gas top flow	1360 l/h
Shielding gas backing flow	340 l/h
Focal distance	150 mm
Focal diameter	0.45 mm
Focal position[a]	0 mm

Table 1: *The parameter values of the experiments.*

[a]Relative to top surface of the sample

Solidus temp. [9, 10, 11]	T_s	852 K		
Liquidus temp. [9, 10, 11]	T_l	911 K		
Boiling temp.[a] [8]	T_b	1363 K		
Latent heat [10]	dH	$3.58 \cdot 10^6$ J/kg		
Dynamic viscosity [11]	μ	$1.05 \cdot 10^6$ kg/(m s)		
Density[b] [10]	ρ	2454 kg/m^3		
Thermal conductivity [8, 9]	λ	$0.06230T + 102.2$	W/(m K)	$T_r \leq T \leq T_s$
		$-4.800 \cdot 10^{-4}T^2 - 0.2178T + 689.3$		$T_s < T \leq T_l$
		$0.03300T + 59.99$		$T_l < T \leq T_b$
Specific heat[c] [9]	C_p	$0.4520T + 773.6$	J/(kg K)	$T_r \leq T \leq T_s$
		1097		$T_s < T \leq T_l$
		$-7.400 \cdot 10^{-3}T^2 + 12.04T - 3732$		$T_l < T \leq T_b$

Table 2: *The material parameters of AA5182 used in the FEM model.*

[a]Boiling temperature of Mg
[b]Averaged over temperature
[c]Excluding the latent heat

chip. In this way only the light from the illumination source, which contains the geometrical information of the weld zone, reaches the camera chip, while the interfering optical emissions of the welding process itself are strongly reduced.

The experiments were conducted using a 4 kW Trumpf THL4006D CW Nd:YAG laser in combination with a 0.60 mm core optical fiber. A standard Trumpf BEO70 welding head with a 200 mm collimator lens and a 150 mm focussing lens were used, resulting in a focal diameter of 0.45 mm. For illumination, a 10 W Laserwave LW-3010-HB CW fiber coupled diode laser source, with a central wavelength of 808 nm, was used. The welding head was moved over the sample using a gantry type manipulator. Experiments were carried out using a laser power ranging from 2.5 kW to 4.0 kW and welding speeds ranging from 100 mm/s to 200 mm/s. Table 1 gives an overview of all parameters used during welding.

Model Validation

The described model was implemented for a AA5182 aluminium alloy, using the Comsol Multiphysics^{TM}package. In Table 3 the chemical composition of AA5182-H111/O is given.

To obtain useful simulation results, it is essential that accurate material parameter data are available. Since the thermal conductivity and the specific heat vary considerably over temperature, the temperature dependency of these parameters is taken into account in the FEM model. In Figure 5 and Table 2 these data are given.

Figure 3 shows a FEM model result for a welding

Element	Content [mass%]
Mg	4.90
Mn	0.26
Cu	0.11
Si	0.08
Ti	0.01
Al	Bal.

Table 3: *The chemical composition of the AA5182-O/H111 base material (information provided by Corus).*

speed of 100 mm/s and a laser power of 2500 W. Figure 4 shows an in-situ camera image of the welding process using these same welding parameters. In these camera images the melt pool contour can be distinguished clearly. By comparing the size and shape of the melt isotherm in the FEM model result with the melt contour in the camera images, the accuracy of the calculated temperature field can be verified.

Three model variations were compared with experimental data (Figure 6). In model I, the thermal and hydrodynamical equations were solved using constant values of the thermal conductivity and the specific heat over the entire temperature range: $\lambda = 120$ W/(m K) and $c_p = 1066$ J/(kg K). Also the effect of latent heat was not taken into account ($dH = 0$).

In model II, again the thermal conductivity was constant. However the latent heat was taken into account by adapting the specific heat between the solidus and the liquidus temperatures as shown in

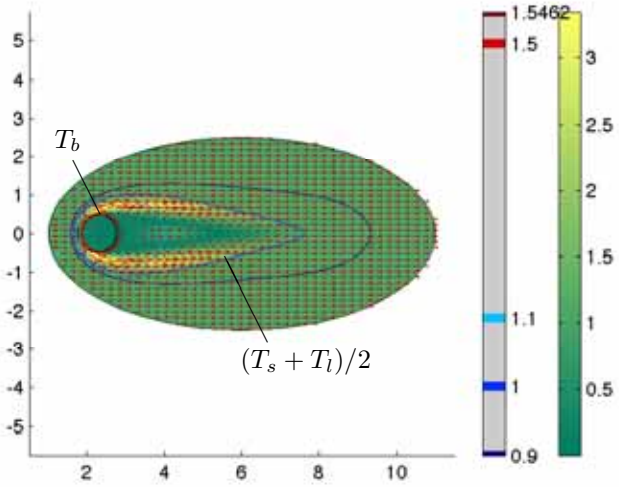

Figure 3: *FEM calculation of the temperature distribution and the flow field for a welding speed of 100 mm/s and a laser power of 2500 W in dimensionless units, with L_0 = 0.6 mm (observed keyhole diameter) and T_0 = 881.5 K (average of solidus and liquidus temperature).*

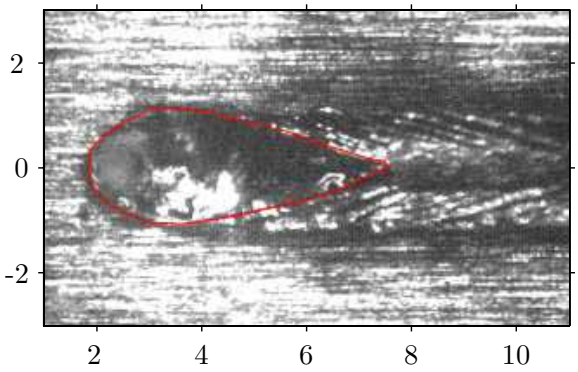

Figure 4: *Coaxial camera image of a laser weld with a welding speed of 100 mm/s and a laser power of 2500 W in dimensionless units, with L_0 = 0.6 mm (observed keyhole diameter). The melt contour is encircled.*

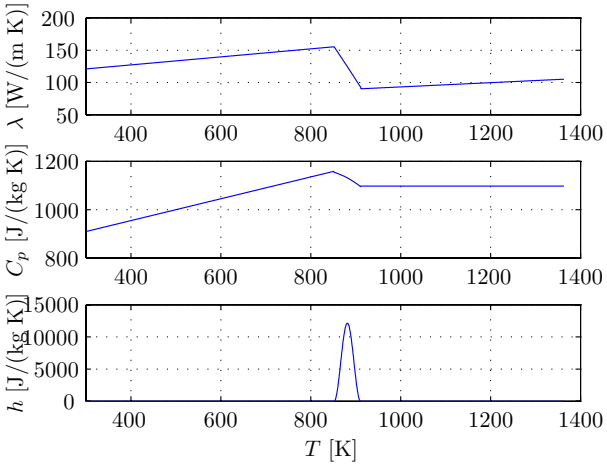

Figure 5: *The thermal conductivity λ [8, 9], the specific heat C_p (excluding the latent heat) [9] and the latent heat h [10, 5] of AA5182 as a function of temperature T.*

Figure 5 and Equation 3. Outside this temperature range, the specific heat was again constant.

Model III includes temperature dependant values of the thermal conductivity and the specific heat, as given in Figure 5 and Table 2, including the latent heat.

For all simulations it was assumed that maximally 50% of the laser energy was absorbed by the material. If the local temperature in the model reached the boiling temperature, the temperature was artificially clipped, effectively reducing the amount of absorbed radiation. Figure 6 shows the melt contours as predicted by the three 2D models, together with contours of the melt pool at the top surface as observed with the monitoring system.

Results and Discussion

Figure 6 shows that Model I cannot make an accurate prediction of the melt pool size and shape. The camera images show a typical V-shaped tail of the melt contour. This phenomenon is typically caused by the latent heat of the solid-liquid phase transition [5], illustrated by the fact that both Model II and III quite accurately predict this V-shape. This demonstrates the importance of incorporating this latent heat in welding models. Model III results in the most accurate predictions of the melt contour, although the predictions of Model II are nearly as good. Apparently, the temperature dependence of the material parameters only has a small influence on the model results.

The camera images show that an increase of the laser power results in a decrease in melt pool length at the top surface (Figure 7). This tendency is not accurately predicted by the models. This can be the result of a different keyhole shape due to a stronger ablation pressure at the front keyhole wall, which changes the 3D flow field in the melt pool. This changed keyhole shape also will affect the amount of absorbed laser power. These effects cannot be modelled easily using the current 2D model. For a

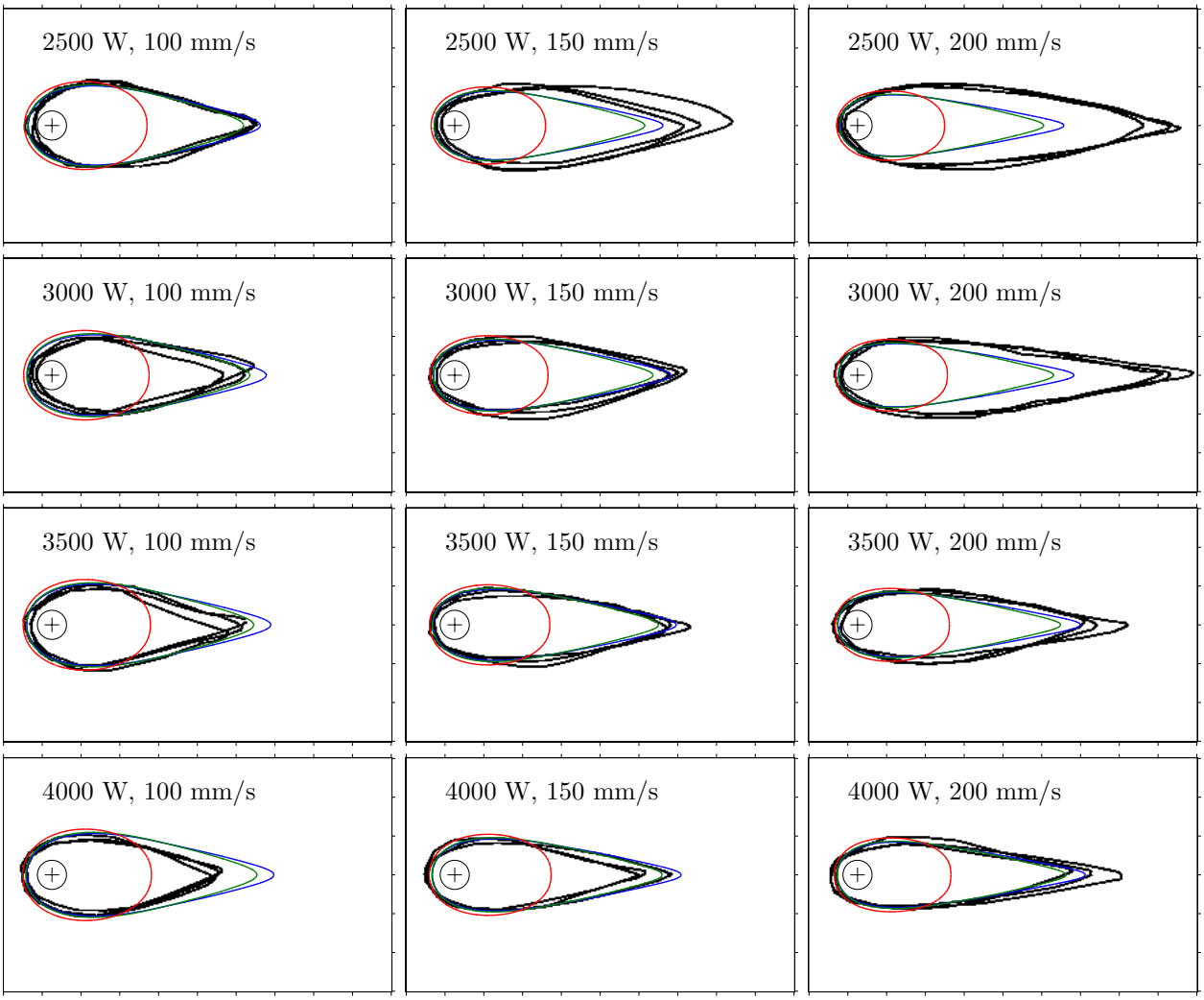

Figure 6: *The melt contours as predicted by Model I (■), Model II (■) and Model III (■), compared to the edges of the melt pool observed in the camera images (■), for different values of the laser power and the welding speed. The circle with the cross indicates the position of the laser spot.*

similar reason, the increase of the melt pool length with an increasing welding speed is not accurately predicted. However, the melt pool width and thus the resulting weld bead width are predicted accurately by all three models (Figure 8).

The results of Model III show that the region with maximum speed of the melt flow is located just next to the keyhole in the thin melt film, which is pushed backwards into the melt pool. The velocity in that region is about three times the welding speed (Figure 3). In the melt pool a recirculation flow is generated, with a back flow of melt towards the keyhole along the centerline of the weld. This flow might be responsible for the occasional keyhole collapses, which are observed in the camera images.

Conclusions

The main conclusions that can be drawn are:

1. Incorporation of the latent heat in welding models is essential to make accurate predictions of the temperature distribution and the flow field.

2. The use of temperature dependent material parameters increases the model accuracy, but the improvement is limited.

3. Experimental data show that a decrease in laser power increases the melt pool length, which is not seen in the model results. This effect is believed to be caused by a change

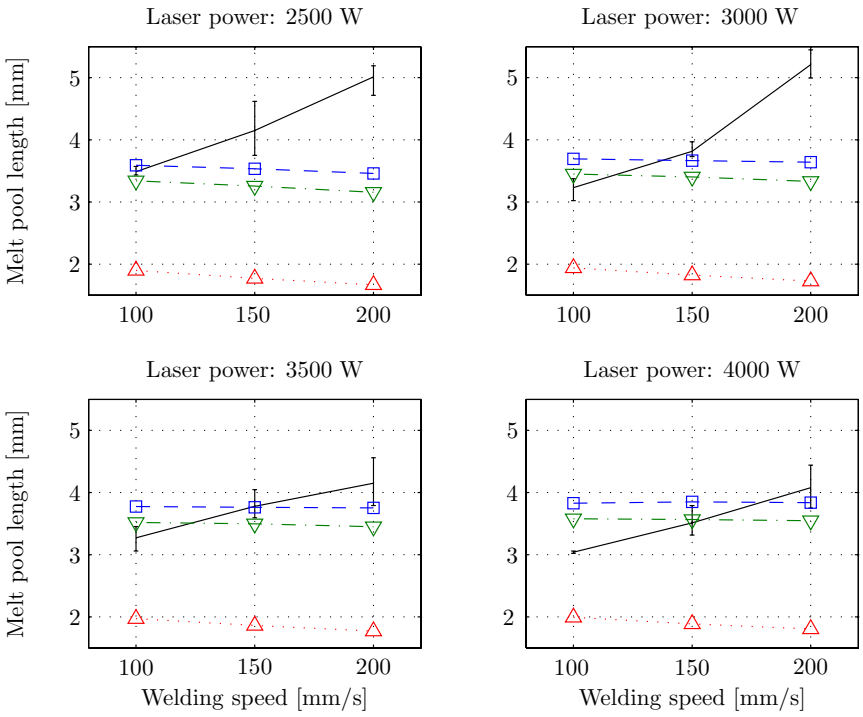

Figure 7: *The length of the melt pool as predicted by Model I (△), Model II (▽) and Model III (□), compared to the length observed in the camera images (–).*

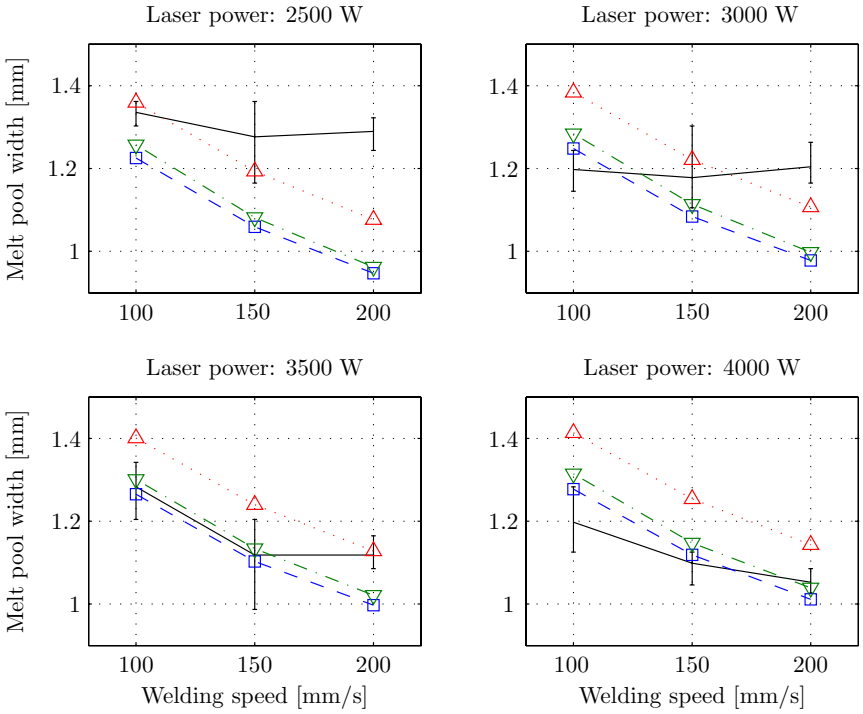

Figure 8: *The width of the melt pool as predicted by Model I (△), Model II (▽) and Model III (□), compared to the width observed in the camera images (–).*

of the 3D keyhole geometry resulting in an alteration of the 3D flow and the laser energy absorption and can therefore not be included in the 2D model.

4. The models show a melt flow with maximum velocities in the order of three times the welding speed around the keyhole. Along the weld centerline the melt flows rapidly backwards to the keyhole and this might be a cause for the occasional keyhole collapses which are observed.

Acknowledgements

This research was carried out under the project numbers MC8.02115 and MC8.02116 in the framework of the Strategic Research Program of the Netherlands Institute of Metals Research (www.nimr.nl). The authors wish to thank Corus for their continuing support.

References

[1] P.G. Klemens. Heat balances and flow conditions for electron beam and laser welding. *Journal of Physics D: Applied Physics*, 47: 2181 – 2194, 1976.

[2] A.F.H. Kaplan. A model of deep penetration laser welding based on calculation of the keyhole profile. *Journal of Physics D: Applied Physics*, 27:1805 – 1814, 1994.

[3] W.W. Duley. *Laser Welding*. John Wiley and Sons, Inc, 1999.

[4] P. Li, H. Hyungson, and J. Mazumder. Modeling Laser Keyhole-Welding with Adaptive Mesh Refinement. *Proceedings of ICALEO '05*, pages 512 – 517, 2005.

[5] D.F. de Lange, S. Postma, and J. Meijer. Modelling and Observation of Laser Welding: The Effect of Latent Heat. *Proceedings of ICALEO '03*, 2003.

[6] D. Schuöcker and A.F.H. Kaplan. Overview over modelling for laser applications. *Proceedings of SPIE '94*, 2207:236 – 247, 1994.

[7] B.J. Aalderink, R.G.K.M. Aarts, J.B. Jonker, and J. Meijer. Experimental Observations of the Laser Keyhole Welding Process of AA5182. *Proceedings of ICALEO '05*, pages 832 – 836, 2005.

[8] *CRC Handbook of Chemistry and Physics*. CRC Press, 84 edition, 2003.

[9] J. Sengupta, S.L. Cockcroft, D.M. Maijer, and A. Larouche. Quantification of temperature, stress, and strain fields during the start-up phase of direct chill casting process by using a 3D fully coupled thermal and stress model for AA5182 ingots. *Materials Science and Engineering A*, 397:157 – 177, 2005.

[10] K.C. Mills. *Recommended values of thermophysical properties for selected commercial alloys*. Woodhead Publishing Limited, first edition, 2002.

[11] *ASM Specialty Handbook - Aluminum and Aluminum Alloys*. ASM International, first edition, 1993.

Meeting the Author

B.J. Aalderink is a PhD researcher, working for the Netherlands Institute for Metals Research (NIMR). He holds a M.Sc. in Applied Physics and his main interests lie in the field of systems and control engineering, robotics, sensor design and laser material processing technology.